

DEEPIINSIGHT: A GENERAL FRAMEWORK FOR INTERPRETING WIDE-BAND NEURAL ACTIVITY

Markus Frey^{1,2,*}, Sander Tanni³, Catherine Perrodin⁴, Alice O'Leary³, Matthias Nau^{1,2}, Jack Kelly⁵, Andrea Banino⁶, Christian F. Doeller^{1,2,7}, and Caswell Barry^{3,7,*}

¹Kavli Institute for Systems Neuroscience, Centre for Neural Computation, The Egil and Pauline Braathen and Fred Kavli Centre for Cortical Microcircuits, NTNU, Norwegian University of Science and Technology, Trondheim, Norway

²Max-Planck-Institute for Human Cognitive and Brain Sciences, Leipzig, Germany

³Cell & Developmental Biology, UCL, London, United Kingdom

⁴Institute of Behavioural Neuroscience, UCL, London, United Kingdom

⁵Open Climate Fix, London, United Kingdom

⁶DeepMind, London, United Kingdom

⁷Joined senior authors

ABSTRACT

Rapid progress in technologies such as calcium imaging and electrophysiology has seen a dramatic increase in the size and extent of neural recordings, yet their interpretation still depends on time-intensive manual operations. Decoding provides a means to infer the information content of such recordings but typically requires highly processed data and prior knowledge of variables. Here, we developed DeepInsight - a deep-learning-framework able to decode sensory and behavioural variables directly from wide-band neural data. The network requires little user input and generalizes across stimuli, behaviours, brain regions, and recording techniques. Critically, once trained, it can be analysed to determine elements of the neural code that are informative about a given variable. We validated this approach using data from rodent auditory cortex and hippocampus, identifying a novel representation of head direction encoded by CA1 interneurons. Thus, we present a robust, user-friendly tool for characterising and decoding neural recordings in an automated way. Code is available at <https://github.com/CYHSM/DeepInsight>.

INTRODUCTION

A central aim of neuroscience is deciphering the neural code, understanding the neural representation of sensory features and behaviours, as well as the computations that link them. The task is complex, and although there have been notable successes - such as the identification of orientation selectivity in V1 ([Hubel and Wiesel, 1959](#)) and the representation of self-location provided by hippocampal place cells ([O'Keefe and Dostrovsky, 1971](#)) - progress has been slow. Neural activity is high dimensional and often sparse, while the available datasets are typically incomplete, being both temporally and spatially limited. This problem is compounded by the fact that the code is multiplexed and functionally distributed ([Walker et al., 2011](#)). As such, activity in a single region may simultaneously represent multiple variables, to differing extents, across different elements of the neural population. Taking the entorhinal cortex for example, a typical electrophysiological recording might contain spike trains from distinct cells predominantly encoding head direction, self-location, and movement speed via their firing rates ([Sargolini et al., 2006](#); [Kropff et al., 2015](#); [Hafting et al., 2005](#)), while other neurons have more complex composite representations ([Hardcastle et al., 2017](#)). At the same time, information about speed and location can also be identified from the local field potential (LFP) ([McFarland et al., 1975](#)) and the relative timing of action potentials ([O'Keefe and Recce, 1993](#)). Fundamentally, although behavioural states and sensory stimuli can generally be considered to be low dimensional, finding the mapping between noisy neural

representations and these less complex phenomena is far from trivial.

Historically, the approach for identifying the correspondence between neural data and external observable states – stimuli or behaviour – has been one of raw discovery. An experimenter, guided by existing knowledge, must recognise the fact that activity covaries with some other factor. Necessarily this is an incremental process, favouring identification of the simplest and most robust representations, such as the sparse firing fields of place cells (**Muller et al., 1987**). Recent advances in machine learning suggest an alternative strategy. Artificial neural networks (ANNs) trained using error backpropagation regularly exceed human-level performance on tasks in which high dimensional data is mapped to lower dimensional labels (**Krizhevsky et al., 2012; Mnih et al., 2015**). Indeed, these tools have successfully been applied to *processed* neural data - accurately decoding behavioural variables from observed neural firing rates (**Glaser et al., 2017; Tampuu et al., 2018**). However, the true advantage of ANNs is not their impressive accuracy but rather the fact that they make few assumptions about the structure of the input data and, once trained, can be analysed to determine which elements of the input are most informative. Viewed in this way ANNs potentially provide a means to accelerate the discovery of novel neural representations.

To test this proposal, we developed a convolutional neural network (**LeCun et al., 2015**) able to take minimally processed, wide-band neural data as input and output predicted continuous regression variables. In the first instance, we trained the model with unfiltered and clustered electrophysiological recordings made from the CA1 pyramidal cell layer in freely foraging rodents. As expected, the network accurately decoded the animals' location, speed, and head direction explicitly without spike sorting or additional user input. Analysis of the trained network showed that it had 'discovered' place cells (**O'Keefe and Dostrovsky, 1971; O'Keefe and Nadel, 1978**) - frequency bands associated with pyramidal waveforms being highly informative about self-location. Equally, it successfully recognized that theta-band oscillations in the LFP were informative about running speed (**McFarland et al., 1975; Jeewajee et al., 2008**). Unexpectedly, the network also identified a population of CA1 interneurons that encoded information about head direction. We corroborated this observation using conventional tools, confirming that the firing rate of these neurons was modulated by facing-direction - a previously unreported relationship. Subsequently, to demonstrate the generality of this approach, we applied the same architecture to electrophysiological data from auditory cortex as well as two-photon calcium imaging data (**Stosiek et al., 2003**) acquired while mice explored a virtual environment.

Our model differs markedly from conventional decoding methods which typically use Bayesian estimators (**Zhang et al., 1998**) in conjunction with highly processed neural data. In the case of extracellular recordings, this usually implies that time-series are filtered and processed to detect action potentials which are then assigned to specific neurons. It is on this basis that expected neural activity as a function of the decoded variables are calculated. Necessarily this approach potentially introduces biases in spike sorting (**Wood et al., 2004**) – favouring waveforms that are easily discriminated, being dependent on the algorithm used (**Pachitariu et al., 2016; Chung et al., 2017; Lee et al., 2017**), and generally changing with the operator's subjective preferences (**Harris et al., 2000**). More importantly, accurate calculation of prior expectations regarding the way in which the data varies with the decoded variable – an essential component of Bayesian decoding – requires considerable knowledge about the neural signal being studied. In contrast, the flexible, general-purpose approach we describe here requires few assumptions and – once trained - can be interrogated to inform the discovery of novel neural representations.

RESULTS

Accurate decoding of self-location from CA1 recordings

In the first instance we sought to evaluate our network-based decoding approach on well characterised neural data with a clear behavioural correlate. To this end we used as input extracellular electrophysiological signals recorded from hippocampal region CA1 in five freely moving rats - place cells from this area being noted for their spatially constrained firing fields that convey considerable information about an animals self-location (**O'Keefe and Dostrovsky, 1971; Muller et al., 1987**). Animals were bilaterally implanted with 32 tetrodes and, after recovery and screening, 128 channel wide-band (0Hz to 15000 Hz sampled at 30kHz) recordings were made while the rats foraged in a 1.25 x 1.75m arena for approximately 40 minutes (see methods). Raw electrophysiological data were decomposed using Morlet wavelets to generate a three-dimensional representation depicting time, channels, and frequencies from 2Hz to 15000Hz (Figure 1A) (**Torrence and Compo, 1998**). Using the wavelet coefficients as inputs, the model was trained in a supervised-fashion using error backpropagation with the X and Y coordinates of the animal as regression targets. In particular, the model makes use of 2D convolutions, sharing weights across channels and time (Figure 1B, see also Methods and Table S1).

The model accurately decoded position from the unprocessed neural data in all rats, providing a continuous estimate of location with an average error less than 10% of the environment's length. This demonstrates that, as expected, the network was able to identify informative signals in the raw neural data (Mean error 17.31cm \pm 4.46cm; Median error 11.40cm \pm 3.82cm; Chance error 65.03cm \pm 6.91cm; Figure 1C,D). To provide a familiar benchmark, we applied a standard Bayesian decoder (**Zhang et al., 1998; Ólafsdóttir et al., 2015**) to the spiking data from the same datasets (see methods). To this end, action potentials were identified, clustered, manually curated, and spike time vectors were used to decode location - data contained in the local field potential (LFP) was discarded. Notably our CNN approach was consistently more accurate than the Bayesian decoder, exceeding its performance in all animals (Bayesian mean error 23.38cm \pm 4.35cm; network error 17.31cm \pm 4.46 cm; Wilcoxon signed-rank test: T=18, p=0.0001) also outperforming a linear support vector machine trained on the full data set (53.6cm \pm 14.77cm; Figure 1E). Indeed, the relative advantage over the Bayesian decoder increased further when the number of channels used for decoding was downsampled to simulate smaller recordings (linear regression Wald-test, s=-0.65, p=1.83e-10; Figure 1G). Notably, the model achieved a similar decoding performance with twenty tetrodes (80 channels, 23.45cm \pm 3.15cm) as the Bayesian decoder reached with the full data set (128 channels, 23.25cm \pm 2.79cm, Figure 1G). The high accuracy and efficiency of the model suggest that our model utilizes additional information contained in the LFP as well as from sub-threshold spikes and those that were not successfully clustered. Note that neither method has access to the animals' position at the previous timestep as both are effectively feed-forward methods, though the Bayesian decoder incorporates prior information about historic dwell locations and the network implicitly has access to this information as well.

To better understand which elements of the raw neural data the network used, we retrained our model using datasets limited to just the LFP (<250Hz) and just the spiking data (>250Hz). In both cases, the network accurately decoded location (spikes-only (CNN-Spikes) mean error 17.23cm \pm 4.69cm; LFP-only (CNN-LFP) mean error, error 24.24cm \pm 6.00cm; Figure 1E), indicating that this framework is able to extract information from varied electrophysiological sources. Consistent with the supposed higher information content of action potentials, the spikes-only network was considerably more accurate than the LFP-only network (Wilcoxon signed-rank test: T=0, p=1.22e-

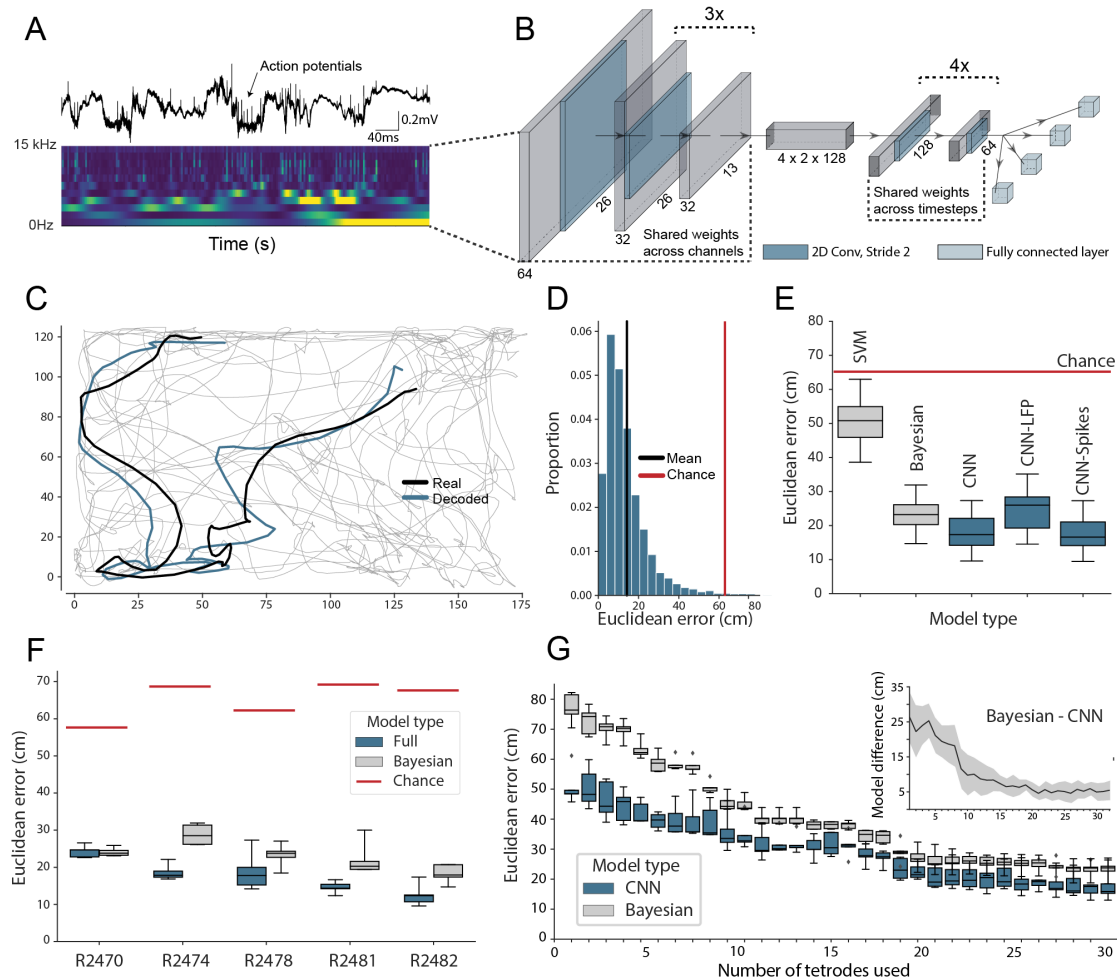


Figure 1: Accurate decoding of self-location from unprocessed hippocampal recordings. A) Top, a typical 'raw' extracellular recording from a single CA1 electrode. Bottom, wavelet decomposition of the same data, power shown for frequency bands from 2Hz to 15kHz (bottom to top row). B) At each timestep wavelet coefficients (64 time points, 26 frequency bands, 128 channels) were fed to a deep network consisting of 2D convolutional layers with shared weights, followed by a fully-connected layer with a regression head to decode self-location; schematic of architecture shown. C) Example trajectory from R2478, true position (black) and decoded position (blue) shown for 3s of data. Full test-set shown in [Video 1](#). D) Distribution of decoding errors from trial shown in (C), mean error ($14.2\text{cm} \pm 12.9\text{cm}$, black), chance decoding of self-location from shuffled data ($62.2\text{cm} \pm 9.09\text{cm}$, red). E) Across all five rats, the network (CNN) was more accurate than a machine learning baseline (SVM) and a Bayesian decoder (Bayesian) trained on action potentials. This was also true when the network was limited to high frequency components ($>250\text{Hz}$, CNN-Spikes). When only local frequencies were used ($<250\text{Hz}$, CNN-LFP), network performance dropped to the level of the Bayesian decoder (distributions compiled from five cross-validations). F) Decoding accuracy for individual animals, the network outperformed the Bayesian decoder in all cases. G) The advantage of the network over the Bayesian decoder increased when the available data was reduced by downsampling the number of channels (data from R2478). Inset shows the difference between the two methods.

05), although the LFP-only network was still comparable with the spike-based Bayesian decoder (Bayesian 23.38cm \pm 4.35cm; LFP 24.24cm \pm 6.00cm; Wilcoxon signed-rank test: T=136, p=0.475).

Simultaneous decoding of multiple factors

The hippocampal representation of self-location is arguably one of the most readily identifiable neural codes - at any instance a small number of sparsely active neurons are highly informative. To provide a more stringent test of the network's ability to detect and decode behavioural variables from unprocessed neural signals, we retrained with the same data but simultaneously decoded position, speed, and head-direction within a single model. CA1 recordings are known to incorporate information about these additional factors but their representation is less pronounced than that for self-location. Thus, the spatial activity of place cells is known to be weakly modulated by head direction (Jercog et al., 2019; Yoganarasimha et al., 2006), while place cell firing rates and both the frequency and amplitude of theta, a 7-10Hz LFP oscillation, are modulated by running speed (McFarland et al., 1975; Jeewajee et al., 2008). In this more complex scenario decoding was accomplished by replicating the final fully connected layer of the network, one layer for each variable, with the provision of appropriate loss functions - cyclical mean absolute error for head direction and mean absolute error for speed (see Methods). All three variables were decoded simultaneously and accurately (Position, 17.78cm \pm 4.96cm; Head Direction, 0.80rad \pm 0.18rad; Speed 4.94cm/s \pm 1.00cm/s; Figure 2A & Video 1), with no meaningful decrement in performance relative to the simpler network decoding only position (position-only model 17.31cm \pm 4.46; combined model 17.78cm \pm 4.96cm; Wilcoxon signed-rank test: T=116, p=0.2108). Indeed, comparison of the R^2 -score metric from the fully trained network - a measure which represents the portion of variance explained and is independent of the loss function - indicated that mean decoding performance was above 0.6 for all three behaviours (R^2 -score Position 0.86 \pm 0.08, Head Direction 0.60 \pm 0.12, Speed 0.72 \pm 0.14, Chance R^2 -score Position -0.14 \pm 0.13, Head Direction 0.04 \pm 0.11, Speed -0.16 \pm 0.22) (Figure 2B). Thus, the network was able to effectively access multiplexed information embedded in minimally processed neural data.

Interrogation of electrophysiological recordings

Although the network supports accurate decoding of self-location from electrophysiological data, this was not our main aim. Indeed, our primary goal for this framework was to provide a flexible tool capable of discovering and characterising sensory and behavioural variables represented in neural data - providing insight about the form and content of encoded information. To this end, in the fully trained network, we used a shuffling procedure to estimate the influence that each element of the 3D input (frequencies x channel x time) had on the accuracy of the decoded variables (see Methods). Since this approach does not require retraining it provides a rapid and computationally efficient means of assessing the contribution made by different frequency bands, electrodes, and time points.

Turning first to position decoding, we saw that the adjacent 469Hz and 663Hz frequency bands were by far the most influential - together accounting for more than 42% of the information about self-location derived from the electrophysiological data (Figure 3A). Since these recordings were made from CA1, we hypothesized that these frequencies corresponded to place cell action potentials. To confirm this hypothesis - and demonstrate that it was possible to objectively use this network-based approach to identify the neural basis of decoded signals - we applied the following approach (see Methods): First, using data from R2478, we isolated the waveforms of place cells (n=123) and interneurons (n=51) which were identified using a conventional approach (Pachitariu et al.,

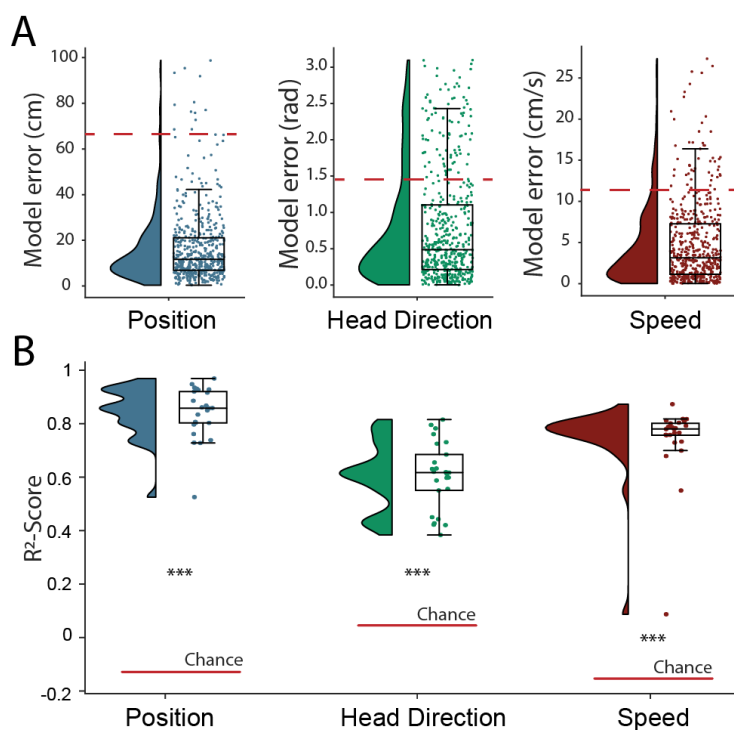


Figure 2: Simultaneous decoding of multiple variables from hippocampal data.

A) Position, head direction, and running speed were accurately decoded in concert by a single network. Data from all five animals, each point indicates an error for a single sample. The red dashed line indicates the chance level obtained by shuffling the input relative to the output while fully retraining the model.

B) R^2 -scores, a loss-invariant measure of model performance - ranging from 1 (perfect decoding) to negative infinity - allowing performance to be compared between dissimilar variables. Data as in (A), each point corresponds to one of five cross-validations within each of five rats

2016). Second, for these two groups, we calculated the relative representation of the 26 frequency bands in their waveforms. We found that the highly informative 469Hz and 663Hz bands were the dominant components of place cell action potentials and that in general the power spectra of these spikes strongly resembled the frequency influence plot for position decoding (Spearman rank-order correlation $\rho=0.84$, $p=7.63e-08$; Figure 3B). In contrast, interneurons - which typically have a shorter after-hyperpolarisation than pyramidal cells (English et al., 2017) - were characterised by higher frequency components (Figure 3B, Mann-Whitney rank test interneuron vs. pyramidal, $U=1009.5$, $p=2.47e-13$), with the highest power at 5304Hz and 3750Hz, bands that were considerably less informative about self-location (Figure 3A).

Since the frequencies associated with pyramidal waveforms were the most informative, this indicated that the network had correctly identified place cells as the primary source of spatial information in these recordings. To corroborate this, we used the same data and for each channel eliminated power in the 469Hz and 663Hz frequency bands at time points corresponding to either place cell or interneuron action potentials. As expected, position decoding was most strongly affected by removal of the place cell time points (Wilcoxon signed-rank test: $T=1497$, $p=2.86e-08$; Figure 3C). Using the same shuffling method we also analysed how informative each channel was about self-location (Figure S3A). In particular, we found that the number of place cells identified on a tetrode from the spike sorted data was highly correlated with the tetrode's spatial influence (Spearman rank-order correlation $\rho=0.71$, $p=5.11e-06$) and that the overall distribution of both number of place cells and spatial influence followed a log-normal distribution (Shapiro-Wilk test on log-transformed data, number of place cells, $W=0.79$, $p=3.59e-05$; tetrode influence $W=0.59$, $p=3.04e-08$; Figure S3B). In sum, this analysis correctly identified that the firing rates of both place cells and interneurons are informative about an animal's location, place cells more so than interneurons (Wilent and Nitz, 2007). The analysis also highlighted the spatial activity of place cells, pointing to the stable place fields as a key source of spatial information.

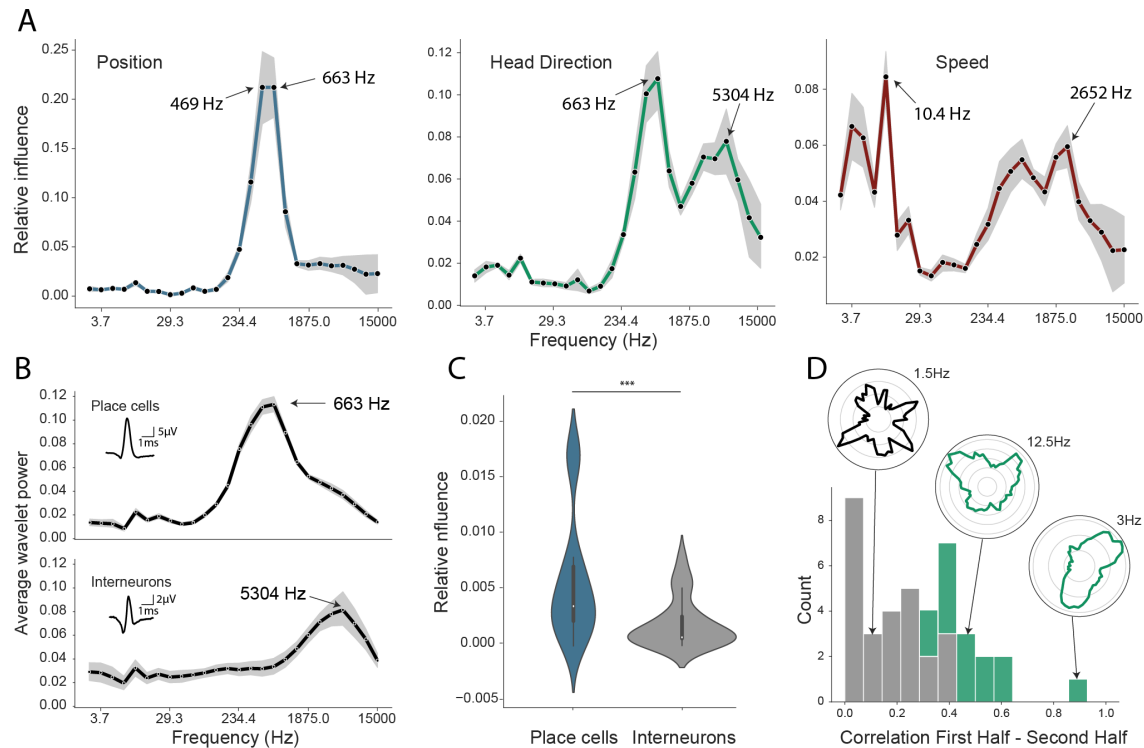


Figure 3: Analysis of trained network identifies informative elements of the neural code.

(A) A shuffling procedure was used to determine the relative influence of different frequency bands in the network input. Left, the 469Hz and 663Hz components - corresponding to pyramidal cell action potentials - were highly informative about animals' positions. Middle, both pyramidal cells and interneurons (5304Hz) carried information about head direction. Right, several frequency bands were informative about running speed, including those associated with the LFP (10.4Hz) and action potentials. Data from all animals. (B) Wavelet coefficients of place cell (top) and interneuron (bottom) waveforms are distinct and correspond to frequencies identified in A. Inset, average waveforms. Data from R2478. (C) Frequency bands associated with place cells (469 & 663Hz) were more informative about position than those associated with interneurons (5304 Hz) - their elimination produced a larger decrement in decoding performance ($p < 0.001$). (D) A subset of CA1 interneurons stably encodes head direction (Pearson correlation between 1st & 2nd half trial). Green indicates cells with significant ($p < 0.01$) Kullback-Leibler divergence vs. uniform circle and significant stability between trial halves ($n = 14/51$). Inset, example polar ratemaps. Data from R2478.

CA1 interneurons are modulated by head direction

Next, having validated our approach for spatial decoding, we examined the basis upon which the network was able to decode head direction. Although place cells primarily provide an allocentric spatial code, their infield firing rate is known to be modulated by heading direction (Muller et al., 1994; Rubin et al., 2014). Consistent with the presence of this directional code, we again saw that the most influential frequencies for head direction decoding were those associated with pyramidal cells (469Hz and 663Hz; Figure 3A). However, the distribution also incorporated a secondary peak corresponding to the frequencies typical for interneuron waveforms (Spearman rank-order correlation $\rho = 0.76$, $p = 5.71 \times 10^{-6}$). Presubicular interneurons have been shown to be modulated by both head direction and angular velocity (Preston-Ferrer et al., 2016) but to the best of our knowledge no similar responses have been noted in CA1. To establish if interneurons conveyed information about head direction we again used an 'elimination' analysis on data from R2478 - the two frequency bands most strongly associated with interneurons (3750Hz and 5304Hz) were shuffled within each channel's signal at time points when interneuron spikes were present. Consistent with the influence plots, we found that selectively eliminating interneurons degraded the accuracy with which head

direction was decoded (relative influence: 0.089 ± 0.043 , t-test $t=4.16$, $p=0.014$). As a final step, to verify this novel observation we reverted to a standard approach. Specifically, we calculated the directional ratemap for each interneuron using only periods when the animal was in motion ($>10\text{cm/s}$), determined the Kullback-Leibler divergence vs. a uniform circle (Doeller et al., 2010), and applied a shuffling procedure to determine significance - as a whole the population exhibited reliable but weak modulation of interneuronal firing rate by head direction (Kullback-Leibler Divergence ($n=51$): 0.0067 ± 0.009) with 52.9% (27/51) of cells being individually significant ($p<0.01$). Behaviours that are inhomogeneously distributed or confounded can result in spurious neural correlates (Muller et al., 1994). To control for this possibility we repeated the analysis using only data from the centre of the environment ($>25\text{cm}$ from the long sides of the enclosure and $>20\text{cm}$ from the short sides). Additionally, to verify stability, we controlled that ratemaps generated from the first and second half of the trial were correlated (Pearson correlation, $p<0.01$). Under this more rigorous analysis, we confirmed that a sub-population (27.5%, 14/51) of hippocampal interneurons were modulated by head direction, a previously unrecognised spatial correlate (Figure 3D).

Multiple electrophysiological features contribute to the decoding of speed

The frequency influence plots for running speed also showed several local peaks (Figure 3A), that in all cases corresponded to established neural correlates. In rodents, theta frequency and power are well known to co-vary almost linearly with running speed (McFarland et al., 1975; Jeewajee et al., 2008), accordingly analysis of the network identified the 10.4Hz frequency band as the most influential. Similarly, the firing rate of place cells increases with speed, an effect captured by the peak at 663Hz. Interestingly a clear peak is also evident at 2652Hz, indicating that interneuron firing rates are also informative - originating either from CA1 speed cells (Góis and Tort, 2018) or from theta-locked interneurons (Huh et al., 2016). Finally, a 4th peak was evident at 3.66Hz and 5.17Hz, a range that corresponds to type 2 ('atropine sensitive') theta which is present during immobility (Kramis et al., 1975; Sainsbury et al., 1987). To corroborate this conclusion, we calculated the correlation between power in each frequency band and running speed (Supplementary Figure S2), confirming that the latter band showed the expected negative correlation - higher power at low speeds - while the other three peaks were positively correlated.

DeepInsight generalizes across brain regions and recording techniques

As a final step, we sought to determine how well our approach generalised to other recording techniques and brain areas. Addressing the latter point first, we trained the network using electrophysiological recordings (64 channels) from the primary auditory cortex of a freely-moving mouse while pure tone auditory stimuli (4 to 64kHz, duration 200 ms) were played from a speaker (Figure 4A). As above, the raw electrophysiological data was transformed to the frequency domain using Morlet wavelets and this wide-band frequency representation was used as input to the same model. The auditory stimuli - training target - was modelled as a continuous variable with '-1' indicating no tone present and the log-transformed frequency of the sound at all other time points. As expected, this model architecture was also able to accurately decode tone stimuli from auditory cortex (R^2 -scores of 0.734 ± 0.080 , chance model: -0.432 ± 0.682 , Figure 4B,C). Informative frequencies were concentrated around 663Hz and 165Hz, indicating that information content about tone stimuli comes mostly from pyramidal cell activity.

Having shown that the model generalises across different brain areas we wanted to further investigate if it generalizes across different recording techniques. Therefore, in the third set of experiments we acquired two-photon calcium fluorescence data from mouse CA1 while the head-fixed animal

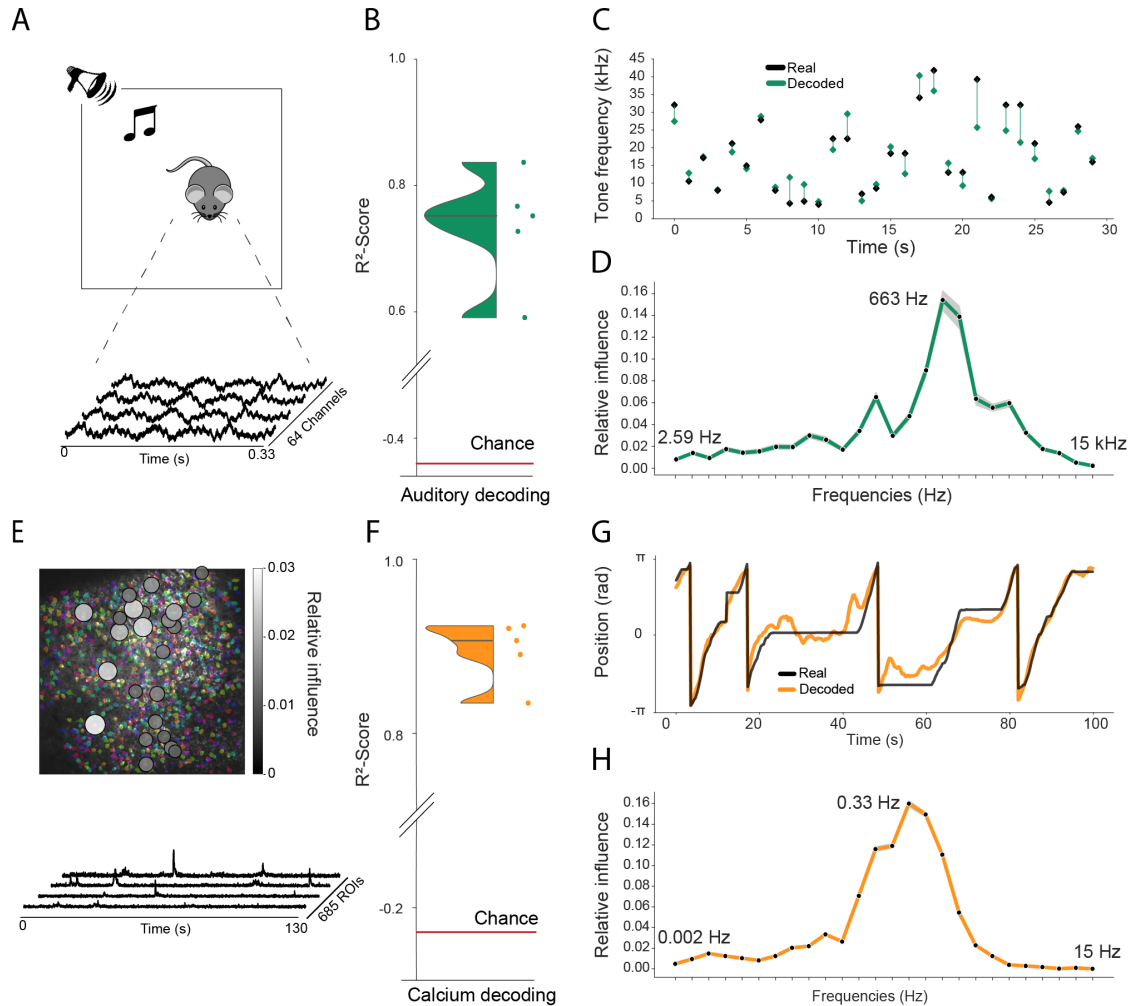


Figure 4: Model generalizes across recording techniques and brain regions

(A) Overview of auditory recording. We recorded electrophysiological signals while the mouse is freely moving inside a small enclosure and is presented with pure tone stimuli ranging from 4kHz to 64kHz. (B) R^2 -score for decoding of frequency tone from auditory cortex (0.73 ± 0.08), chance level is indicated by the red line. (C) An example section for decoding of auditory tone frequencies from auditory electrophysiological recordings, real tone colored in black, decoded tone in green, the line between real and decoded indicates magnitude of error. (D) Influence plots for decoding of auditory tone stimuli, same method as used for CA1 recordings. (E) Calcium recordings from rat running on a linear track in VR. We record from 685 cells and use Suite2p to preprocess the raw images and extract calcium traces which we feed through the model to decode linear position. (F) R^2 -score for decoding of linear position from two-photon CA1 recordings (0.90 ± 0.03), chance level is indicated by the red line. (G) Example trajectory through the virtual linear track (linearized to $[-\pi, \pi]$) with real position (black) and decoded position (orange). (H) Influence plots for decoding of position from two-photon calcium imaging. Note that the range of frequencies is between 0Hz and 15Hz as the sampling rate of the calcium traces is 30Hz.

explored a 230cm virtual track. Raw data was preprocessed to generate denoised activity traces for putative cells ($n=685$ regions of interest), these were then decomposed to a frequency representation using the same wavelet approach as before - only frequency bands between 0Hz and 15Hz being used because of the lower data rate (30Hz) (see methods, Figure 5E). Wavelet coefficients were provided to the network as input with most of the architecture kept the same, only the number of down-sampling steps were increased to account for the large number of ROIs. The network was able to accurately decode the animal's position on the track (mean error: 15.87 ± 16.33 cm, R^2 -scores of 0.90 ± 0.03 vs. chance model -0.05 ± 0.127 , Figure 4F,G). Using the same shuffling technique as before, we generated influence plots indicating the relative information provided by frequencies (Fig 4H) and ROIs (Fig 4E). In the frequency domain, the most informative bands were 0.33Hz and 0.46Hz, mirroring the 1s to 2s decay time of GCaMP6s (Chen et al., 2013). In contrast, informative ROIs were distributed across the field of view with no discernible pattern (Figure 4E) - a result that is expected given the absence of topographic representations in hippocampus (Dombeck et al., 2010).

DISCUSSION

The neural code provides a complex, non-linear representation of stimuli, behaviours, and cognitive states. Reading this code is one of the primary goals of neuroscience - promising to provide insights into the computations performed by neural circuits. However, decoding is a non-trivial problem, requiring strong prior knowledge about the variables encoded and, crucially, the form in which they are represented. Not only is this information often incomplete or absent but a full characterisation of the neural code is precisely the question we seek to solve. Addressing these limitations, we investigated the potential of a deep-learning framework to decode behaviours and stimuli from wide-band, minimally processed neural activity. To this end, we designed a model architecture using simple 2D convolutions with shared weights, omitting recurrent layers. These intentional design choices resulted in a fast, data efficient architecture that could be easily interpreted to discover which elements of the neural code provided information about specific variables - a decrease in network performance was accepted as a trade-off.

In the first instance we validated our approach using the well characterised spatial representations of rodent CA1 place cells. Decoding performance amply exceeded that of a simple Bayesian decoder but importantly the network correctly identified pyramidal cell action potentials as the most informative spatial signal. In a further set of experiments with the same data, we showed that the network was able to identify multiple neural representations of head direction and running speed, including several that were only recently reported and one - interneuron encoding of head direction - that was, as far as we are aware, previously unreported. Finally, we demonstrated the flexibility of this approach, applying the same core network, with adjustments made to the input and output layers, to two-photon calcium data and extracellular recordings from auditory cortex.

In sum, we believe deep-learning based frameworks such as this, constitute a valuable tool for neuroscientists - being able to provide a general overview as to whether a variable is encoded in a data set but also providing detailed information about the nature of that encoding. That is not to say that this approach is a complete substitute for conventional analyses - it merely constrains the search space for variables that might be present and their plausible format. Indeed, we imagine this network might be best used as a first pass analysis, followed by conventional approaches to determine explicitly if a variable is present - much as we did for the interneuron representation of head direction. We note that in principal this network can accept neural data

from most experimental settings, including fMRI and MEG. However, its greatest utility is likely to be evident when applied to wide-band neural data.

METHODS

Tetrode recordings from CA1

Five male Lister Hooded rats were used for this study. All procedures were approved by the UK Home Office, subject to the restrictions and provisions contained in the Animals Scientific Procedures Act of 1986. All rats (333-386 g/13-17 weeks old at implantation) were implanted with two single-screw microdrives (Axona Ltd.) targeted to the right and left CA1 (ML: 2.5 mm, AP: 3.8 mm posterior to bregma, DV: 1.6 mm from dura). Each microdrive was assembled with two 32 channel Omnetics connectors (A79026-001) and 16 eight tetrodes of twisted wires (either 17 μm H HL coated platinum iridium, 90% and 10% respectively, or 12.7 μm HM-L coated Stablohm 650; California Fine Wire), platinum plated to reduce impedance to below 150 k Ω at 1 kHz (NanoZ). After surgery, rats were housed individually on a 12 hr light/dark cycle and after one week of recovery rats were maintained at 90% of free-feeding weight with ad libitum access to water.

Screening was performed from one week after surgery. Electrophysiological data was acquired using Open Ephys recording system (Siegle et al., 2017) and a 64-channel amplifier board per drive (Intan RHD2164). Positional tracking performed using a Raspberry Pi with Camera Module V2 (synchronised to Open Ephys system) and custom software, that localised two different brightness infra-red LEDs attached to amplifier boards on camera images acquired at 30 Hz. During successive recording sessions in a separate screening environment 1.4 x 1.4 m the tetrodes were gradually advanced in 62.5 μm steps until place cells were identified. During the screening session, the animals were often being trained in a spatial navigation task for projects outside the scope of this study.

The experiments were run during the animals' dark period of the L/D cycle. The recording sessions used in this study were around 40 min long, depending on the spatial sampling of the animal, in a rectangular environment of 1.75 x 1.25 m, on the second, third or fourth exposure, varying between animals. The environment floor was black vinyl flooring, it was constructed of 60 cm high boundaries (MDF) colored matt black, surrounded by black curtains on the sides and above. There was one large cue card raised above the boundary and two smaller cue cards distributed on the side of the boundary. Foraging was encouraged with 20 mg chocolate-flavoured pellets (LBS Biotechnology) dropped into the environment by custom automated devices. The recordings used in this study were part of a longer session that involved foraging in multiple other different size open field environments.

Rats were anaesthetised with isoflurane and given intraperitoneal injection of Euthanal (sodium pentobarbital) overdose (0.5 ml / 100 g) after which they were transcardially perfused with saline, followed by a 10% Formalin solution. Brains were removed and stored in 10% Formalin and 30% Sucrose solution for 3-4 days prior to sectioning. Subsequently, 50 μm frozen coronal sections were cut using a cryostat, mounted on gelatine coated or positively charged glass slides, stained with cresyl violet and cleared with clearing agent (Histo-Clear II), before covering with DPX and coverslips. Sections were then inspected using Olympus microscope and tetrode tracks reaching into CA1 pyramidal cell layer were verified.

Interneurons were classified based on waveform shape, minimum firing rate across multiple environments and lack of spatial stability. Specifically, classified interneurons had waveform half-width less than 0.15 ms, maximum ratio of amplitude to trough of 0.4, minimum firing rate of 4

Hz and maximal 0.75 spatial correlation of ratemaps from first and last half of the recording in any environment. Note that we used the spatial stability in order to differentiate interneurons from place cells or grid cells, with no influence on the directional stability of the head direction cell analysis.

Calcium recordings from CA1

All procedures were conducted in accordance to UK Home Office regulations.

One GCaMP6f mouse (C57BL/6J-Tg(Thy1-GCaMP6f)GP5.17Dkim/J, Jacksons) was implanted with an imaging cannula (a 3mm diameter x 1.5mm height stainless-steel cannula with a glass coverslip at the base) over CA1 (stereotaxic coordinates: AP=-2.0, ML=-2.0 from bregma). A 3mm craniotomy was drilled at these coordinates. The cortex was removed via aspiration to reveal the external capsule of the hippocampus. The cannula was inserted into the craniotomy and secured to the skull with dental cement. A metal head-plate was glued to the skull and secured with dental cement. The animal was left to recover for at least one week after surgery before diet restriction and habituation to head-fixation commenced.

Following a period of handling and habituation, the mouse was head-fixed above a styrofoam wheel and trained to run for reward through virtual reality environments, presented on 3 LCD screens that surrounded the animal. ViRMEn software (Aronov and Tank, 2014) was used to design and present the animal with virtual reality linear tracks. Movement of the animal on the wheel was recorded with a rotatory encoder and lead to corresponding translation through the virtual track. During the experimental phase of the training, the animal was trained to run down a 230cm linear track and was required to lick at a reward port at a fixed, unmarked goal location within the environment in order to trigger release of a drop of condensed milk. Licks were detected by an optical lick detector, with an IR LED and sensor positioned on either side of the animal's mouth. When the animal reached the end of the linear track, a black screen appeared for 2 seconds and the animal was presented with the beginning of the linear track, starting a new trial.

Imaging was conducted using a two-photon microscope (resonant scanning vivoscope, Scientifica) using 16x/0.8-NA water-immersion objective (Nikon). GCaMP was excited using a Ti:sapphire laser (Mai Tai HP, Spectra-Physics), operated with an excitation wavelength of 940nm. ScanImage software was used for data collection / to interface with the microscope hardware. Frames were acquired at a rate of 30Hz.

The Suite2p toolbox (Pachitariu et al., 2017) was used to motion correct the raw imaging frames and extract regions of interest, putative cells.

Tetrode recordings from auditory cortex

Sound-evoked neuronal responses were obtained via chronically-implanted electrodes in the right hemisphere auditory cortex of one 17-week-old male mouse (*M. musculus*, C57Bl/6, Charles River). All experimental procedures were carried out in accordance with the institutional animal welfare guidelines and a UK Home Office Project License approved under the United Kingdom Animals (Scientific Procedures) Act of 1986.

During recordings, the animal was allowed to freely move within a 11x21 cm cardboard enclosure, with one wall consisting of an acoustically-transparent mesh panel to allow unobstructed sound stimulation. Acoustic stimuli were delivered via two free-field electrostatic speakers (Tucker-Davis Technologies, FL, USA) placed at ear level, 7 cm from the edge of the enclosure. Recordings were

performed inside a double-walled soundproof booth (IAC Acoustics), whose interior was covered by 4-cm thick acoustic absorption foam (E-foam, UK). Pure tones were generated using MATLAB (Matlab version R2015a; MathWorks, Natwick, MA, USA), and played via a digital signal processor (RX6, Tucker Davis Technologies, FL, USA). The frequency response of the loudspeaker was ± 10 dB across the frequency range used for stimulation. Pure tones of a duration of 200ms (including 5 ms linear rise and fall times) of variable frequencies (4-64 kHz in 0.1 octave increments) were used for stimulation. The tones were presented at 65dB SPL at the edge of the testing box. The 41 frequencies were presented pseudo-randomly, separated by a randomly varying inter-stimulus interval ranging from 500 to 510ms, for a total of 20 repetitions.

Extracellular electrophysiological recordings were obtained using a custom chronically-implanted 64-channel hyperdrive with two 32-channel Omnetics connectors (A79026-001) and 16 individually movable tetrodes (FlexDrive, (Voigts et al., 2013)). Tetrodes were made from 12.7 μm tungsten wire (99.95%, HFV insulation, California Fine Wire, USA) gold-plated to reduce impedance to 200k Ω at 1kHz (NanoZ, Multichannel Systems). Neuronal signals were collected and amplified using two 32-channel amplifier boards (Intan RHD 2132 headstages) and an Open Ephys recording system (Siegle et al., 2017) at 30kHz.

Data Preprocessing

Raw electrophysiological traces as well as calcium traces were transformed to a frequency representation using discrete-wavelet transformation (DWT). We decided to use wavelet transformation instead of windowed Fourier transform (WFT) as we expected a wide range of dominant frequencies in our signal for which the wavelet transformation is more appropriate (Torrence and Compo, 1998). For the wavelet transformation, we used the morlet wavelet:

$$\psi_0(\eta) = \pi^{-\frac{1}{4}} * \exp(i * \omega_0 * \eta) * \exp(-\eta^2/2) \quad (1)$$

with a non-dimensional frequency constant $\omega_0 = 6$. We noticed that downscaling the wavelets improved our model performance, prompting us to use an additional preprocessing step which effectively decreased the sampling rate of the wavelets to $\psi_{SR_{after}} = \psi_{SR_{before}}/M$ by a factor of M . This can also be seen as an additional convolutional layer with a kernel size of M , a stride of M and weights fixed to $\frac{1}{M}$. We performed a hyperparameter search for M with a simplified model and found the best performing model with $M = 1000$, thus effectively decreasing our sampling rate from 30000 to 30.

As additional preprocessing steps we applied channel and frequency wise normalization using a median absolute deviation (MAD) approach. We calculated the median and the corresponding median absolute deviation for each frequency and channel on the training set and normalized our inputs as follows:

$$X_i = \frac{X_i - \tilde{X}_i}{\text{median}(|X_i - \tilde{X}_i|)} \quad (2)$$

where \tilde{X}_i is the median of X_i . This approach turned out to be more robust against outliers in the signal than simple mean normalization. Additional min-max scaling did not further improve performance.

Bayesian decoder

As a baseline model, we used a Bayesian decoder which was trained on manually sorted and clustered spikes. Given a time window T and number of spikes $K = (k_1, \dots, k_N)$ fired by N place cells, we can calculate the probability $P(K|x)$, estimating the number of spikes K at location x :

$$P(K|x) = \prod_{i=1}^N \text{Poisson}(k_i, T\alpha_i(x)) = \prod_{i=1}^N \frac{(T\alpha_i(x))^{k_i}}{k_i!} \quad (3)$$

where $\alpha_i(x)$ is the firing rate of cell i at position x . From this we can calculate the probability of the animal's location given the observed spikes:

$$P(x|K) = P(x) \prod_{i=1}^N \alpha_i(x)^{k_i} \exp(-T \sum_{i=1}^N \alpha_i(x)) \quad (4)$$

where $P(x)$ is the historic position of the animal which we use to constrain $P(x|K)$ to provide a fair comparison to the convolutional decoder. The final estimate of position is based on the peak of $P(x|K)$:

$$\hat{x} = \text{argmax}_x P(x|K) \quad (5)$$

We used the same cross-validation splits as for the convolutional model and calculate the euclidean distance between the real and decoded position. We use a gaussian smoothing kernel with $\sigma = 1.5$ and a bin size of 2cm for binning and smoothing the ratemaps, and use a bin length of 0.5s.

Convolutional neural network

The model takes a three-dimensional wavelet transformed signal as input and uses convolutional layers connected to a regression head to decode continuous behaviour. We use a kernel size of 3 throughout the model and keep the number of filters constant at 64 for the first 8 layers while sharing the weights over the channel axis, while then doubling them for each following layer. For downsampling the input we use a stride of 2, intermixed between the time and frequency dimension (Table S1, Fig 1B). We use 2D-convolutions on a three-dimensional input to lower computational load and GPU memory consumption but also to improve generalization. To achieve this, we share the weights across the channel dimension for the first 8 convolutions and across the time dimension for the last 6 convolutional layers. Sharing the weights across channels prevents overfitting to any channel specific feature, making sure there exists a global representation e.g. of spikes or other prominent oscillations in the local field potential.

We extensively investigated the use of a convolutional long-short-term-memory (LSTM) after the initial convolutions, where we used backpropagation through time on the time dimension. In a simplified model this led to a small decrease in decoding error for the model trained on position. We nevertheless decided to employ a model with only simple convolutions as one important aspect of this model is the simplicity of use for a neuroscientist. Moreover we experimented with using a wavenet (Oord et al., 2016) inspired model directly on the raw electrophysiological signal but noticed that the model using the wavelet transformed input outperformed the wavenet approach by a margin of around 20cm for the positional decoding. The wavenet inspired model was considerably slower to train and therefore a full hyperparameter search could not be performed.

Model training

The model takes as input a three-dimensional wavelet transformed signal corresponding to time, frequency and channels, with frequencies logarithmically scaled between 0Hz-15000Hz. An optimal temporal window of $T=64$ (corresponding to 2.13s) was established by hyperparameter search taking into account the tradeoff between speed of training and model error. We randomly sampled inputs and outputs from the training set. Each input had corresponding outputs for the position (X, Y in cm), head direction (in radians) and speed (in cm/s). We used Adam as our learning algorithm with a learning rate of 0.0007 and stopped training after we sampled 18000 samples, divided into 150 batches for 15 epochs, each batch consisting of 8 samples. During training we multiplied the learning rate by 0.2 if validation performance did not improve for 3 epochs. We performed random hyperparameter search for the following parameters: learning rate, dropout, number of units in the fully connected layer and number of input timesteps. For calculating the chance level we used a shuffling procedure in which the wavelet transformed electrophysiological signal is shifted relative to its corresponding position. After shuffling we trained the model with the same setting as the unshuffled model and for the same number of epochs. The training was performed on one GTX1060 using Keras with Tensorflow as backend.

Model comparison

In order to compare the performance of the network against the Bayesian decoder we simulated both models in a setting with artificially reduced inputs. We used 1 to 32 tetrodes as input for both decoders, with tetrodes taken top to bottom in order of the given tetrode number. The input of run 1 was then comprised of tetrodes 1 to 32, while run 2 used tetrodes 1 to 31. The last run uses only the first tetrode as input to both models. We then retrained both models with the artificially reduced number of tetrodes making sure both models have the same cross-validation splits and report decoding errors as the average of each cross-validation split.

Model evaluation

For adjusting the model weights during training we use different loss terms depending on the behaviour or stimuli which we decode.

$$\mathcal{L}_{ED} = \sqrt{\sum_{i=1}^M (\hat{y}_i - y_i)^2} \quad \mathcal{L}_{MSE} = \frac{1}{M} \sum_{i=1}^M (\hat{y}_i - y_i) \quad \mathcal{L}_{CMAE} = \min[|\hat{y}_i - y_i|, |\hat{y}_i - y_i| + \pi, |\hat{y}_i - y_i| - \pi] \quad (6)$$

For decoding of position from tetrode CA1 recordings we try to minimize the Euclidean loss between predicted and ground truth position (\mathcal{L}_{ED}). We use the mean squared error for the decoding of speed (\mathcal{L}_{MSE}) and the cyclical absolute error for decoding of head direction (\mathcal{L}_{CMAE}). For all other behaviours or stimuli we use \mathcal{L}_{MSE} as the default optimizer.

We decided to use R^2 scores to measure model performance across different behaviours, brain areas and recording techniques. We use the formulation of fraction of variance accounted for (FVAF) instead of the squared Pearson's correlation coefficient. Both terms are based on the fraction of the residual sum of squares and the total sum of squares:

$$R^2 = 1 - \frac{\sum_{i=1}^M (y_i - \alpha \hat{y}_i - \beta)^2}{\sum_{i=1}^M (y_i - \bar{y})^2} \quad (7)$$

with y_i the ground truth of sample i , \hat{y}_i the predicted value and \bar{y} the mean value. Here, Pearson's correlation coefficient tries to maximize R^2 by adjusting α and β while FVAF uses $\alpha = 1$ and $\beta = 0$

(Fagg et al., 2009). This provides a more conservative measure of performance as FVAF requires that prediction and ground truth fit without scaling the predicted values. FVAF in turn is has no lower bound as the prediction can be arbitrarily worse with a given scaling constant (i.e. given a ground truth value of 10, a prediction of 1000 has a lower (worse) R^2 score than a prediction of 100).

Influence maps

To investigate which frequencies, channels or timepoints were informative for the respective decoding we performed a bootstrapping procedure after training the models. For each sample in time we calculated the real decoding error e_o for each behaviour by using the wavelets as input. We then shuffle the wavelets for a particular frequency and re-calculate the error. We then define the influence of a given frequency or channel as the relative change: $\frac{e_s - e_o}{e_o}$ where e_o is the original error and e_s the shuffled error. We repeat this for the channel and time dimension to get an estimate of how much influence each channel or timepoint has on the decoding of a given behaviour.

We also tried calculating sample gradients with respect to our inputs (Simonyan et al., 2013). For this we calculated the derivative w by back-propagation for each sample and with respect to the inputs. In contrast to class saliency maps, we obtain a gradient estimate indicating how much each part of the input strongly drives the regression output. We calculate saliency maps for each sample cross-validated over the entire experiment. For deriving influence maps from the raw gradients we calculate the variance across the time dimension and use this as an estimate of how much influence each frequency band or channel has on the decoding. This method however introduces a lot of high-frequency noise in the gradients, possibly coming from the strides in the convolutional layers used throughout the model (Olah et al., 2017).

AUTHOR CONTRIBUTIONS

CB, JK initial idea for project, MF conceived the network architecture and implemented all neural network models, CB implemented the Bayesian decoder, ST spike sorted the data and classified neurons, ST, CP, AL acquired data, MF, ST, CB, MN, AB, JK, CFD contributed ideas to experiments and analysis, MF, CB wrote the paper with input from all authors.

MF and CFD are supported by the European Research Council (ERC-CoG GEOCOG 724836); CFD's research is also funded by the Max Planck Society; the Kavli Foundation; the Centre of Excellence scheme of the Research Council of Norway – Centre for Neural Computation (223262/F50), The Egil and Pauline Braathen and Fred Kavli Centre for Cortical Microcircuits, and the National Infrastructure scheme of the Research Council of Norway – NORBRAIN (197467/F50); CB funded by Wellcome SRF (212281/Z/18/Z); CP funded by Wellcome Trust (110238/Z/15/Z).

REFERENCES

- David H. Hubel and Torsten N. Wiesel. Receptive fields of single neurones in the cat's striate cortex. *The Journal of Physiology*, 148(3): 574–591, 1959.
- John O'Keefe and Jonathan Dostrovsky. The hippocampus as a spatial map. Preliminary evidence from unit activity in the freely-moving rat. *Brain Research*, 34(1):171–175, November 1971.
- Kerry MM Walker, Jennifer K. Bizley, Andrew J. King, and Jan WH Schnupp. Multiplexed and robust representations of sound features in auditory cortex. *Journal of Neuroscience*, 31(41):14565–14576, 2011.
- Francesca Sargolini, Marianne Fyhn, Torkel Hafting, Bruce L. McNaughton, Menno P. Witter, May-Britt Moser, and Edvard I. Moser. Conjunctive Representation of Position, Direction, and Velocity in Entorhinal Cortex. *Science*, 312(5774):758–762, May 2006.
- Emilio Kropff, James E. Carmichael, May-Britt Moser, and Edvard I. Moser. Speed cells in the medial entorhinal cortex. *Nature*, 523(7561):419–424, July 2015.
- Torkel Hafting, Marianne Fyhn, Sturla Molden, May-Britt Moser, and Edvard I. Moser. Microstructure of a spatial map in the entorhinal cortex. *Nature*, 436(7052):801–806, August 2005.
- Kiah Hardcastle, Niru Maheswaranathan, Surya Ganguli, and Lisa M. Giocomo. A Multiplexed, Heterogeneous, and Adaptive Code for Navigation in Medial Entorhinal Cortex. *Neuron*, 94(2):375–387.e7, April 2017.
- Willard L. McFarland, Herman Teitelbaum, and Elizabeth K. Hedges. Relationship between hippocampal theta activity and running speed in the rat. *Journal of Comparative and Physiological Psychology*, 88(1):324–328, 1975.
- John O'Keefe and Michael L. Recce. Phase relationship between hippocampal place units and the EEG theta rhythm. *Hippocampus*, 3(3): 317–330, 1993.
- Robert U. Muller, John L. Kubie, and James B. Ranck. Spatial firing patterns of hippocampal complex-spike cells in a fixed environment. *Journal of Neuroscience*, 7(7):1935–1950, 1987.
- Alex Krizhevsky, Ilya Sutskever, and Geoffrey E. Hinton. ImageNet Classification with Deep Convolutional Neural Networks. In *Proceedings of the 25th International Conference on Neural Information Processing Systems - Volume 1*, NIPS'12, pages 1097–1105, USA, 2012. Curran Associates Inc. event-place: Lake Tahoe, Nevada.
- Volodymyr Mnih, Koray Kavukcuoglu, David Silver, Andrei A. Rusu, Joel Veness, Marc G. Bellemare, Alex Graves, Martin Riedmiller, Andreas K. Fidjeland, Georg Ostrovski, Stig Petersen, Charles Beattie, Amir Sadik, Ioannis Antonoglou, Helen King, Dharmarajan Kumar, Daan Wierstra, Shane Legg, and Demis Hassabis. Human-level control through deep reinforcement learning. *Nature*, 518(7540):529–533, February 2015.
- Joshua I. Glaser, Raeed H. Chowdhury, Matthew G. Perich, Lee E. Miller, and Konrad P. Kording. Machine learning for neural decoding. *arXiv:1708.00909 [cs, q-bio, stat]*, August 2017. arXiv: 1708.00909.
- Ardi Tampuu, Tambet Matiisen, Hauður Freyja Ólafsdóttir, Caswell Barry, and Raul Vicente. Efficient neural decoding of self-location with a deep recurrent network. *bioRxiv*, January 2018.
- Yann LeCun, Yoshua Bengio, and Geoffrey Hinton. Deep learning. *Nature*, 521(7553):436–444, May 2015.
- John O'Keefe and Lynn Nadel. *The hippocampus as a cognitive map*. Oxford: Clarendon Press, 1978.
- Ali Jeewajee, Caswell Barry, John O'Keefe, and Neil Burgess. Grid cells and theta as oscillatory interference: Electrophysiological data from freely-moving rats. *Hippocampus*, 18(12):1175, 2008.
- Christoph Stosiek, Olga Garaschuk, Knut Holthoff, and Arthur Konnerth. In vivo two-photon calcium imaging of neuronal networks. *Proceedings of the National Academy of Sciences*, 100(12):7319–7324, June 2003.
- Kechen Zhang, Iris Ginzburg, Bruce L. McNaughton, and Terrence J. Sejnowski. Interpreting Neuronal Population Activity by Reconstruction: Unified Framework With Application to Hippocampal Place Cells. *Journal of Neurophysiology*, 79(2):1017–1044, February 1998.
- Frank Wood, Michael J. Black, Carlos Vargas-Irwin, Matthew Fellows, and John P. Donoghue. On the variability of manual spike sorting. *IEEE Transactions on Biomedical Engineering*, 51(6):912–918, 2004.

- Marius Pachitariu, Nicholas Steinmetz, Shabnam Kadir, Matteo Carandini, and Harris Kenneth D. Kilosort: realtime spike-sorting for extracellular electrophysiology with hundreds of channels. *bioRxiv*, page 061481, June 2016.
- Jason E. Chung, Jeremy F. Magland, Alex H. Barnett, Vanessa M. Tolosa, Angela C. Tooker, Kye Y. Lee, Kedar G. Shah, Sarah H. Felix, Loren M. Frank, and Leslie F. Greengard. A Fully Automated Approach to Spike Sorting. *Neuron*, 95(6):1381–1394.e6, September 2017.
- Jin Hyung Lee, David E. Carlson, Hooshmand Shokri Razaghi, Weichi Yao, Georges Goetz, Espen Hagen, Eleanor Batty, E. J. Chichilnisky, Gaute T. Einevoll, and Liam Paninski. YASS: Yet Another Spike Sorter. In *NIPS*, 2017.
- Kenneth D. Harris, Darrell A. Henze, Jozsef Csicsvari, Hajime Hirase, and György Buzsáki. Accuracy of Tetrode Spike Separation as Determined by Simultaneous Intracellular and Extracellular Measurements. *Journal of Neurophysiology*, 84(1):401–414, July 2000.
- Christopher Torrence and Gilbert P. Compo. A Practical Guide to Wavelet Analysis. *Bulletin of the American Meteorological Society*, 79(1): 61–78, January 1998.
- H Freyja Ólafsdóttir, Caswell Barry, Aman B Saleem, Demis Hassabis, and Hugo J Spiers. Hippocampal place cells construct reward related sequences through unexplored space. *eLife*, 4:e06063, June 2015.
- Pablo Jercog, Search Results Web results Yashar Ahmadian, Chris Woodruff, Rajeev Deb-Sen, Larry F. Abbott, and Eric R. Kandel. Heading direction with respect to a reference point modulates place-cell activity. *Nature Communications*, 10(1):1–8, May 2019.
- Doreswamy Yoganasimha, Xintian Yu, and James J. Knierim. Head Direction Cell Representations Maintain Internal Coherence during Conflicting Proximal and Distal Cue Rotations: Comparison with Hippocampal Place Cells. *The Journal of Neuroscience*, 26(2):622–631, January 2006.
- Daniel Fine English, Sam McKenzie, Talfan Evans, Kanghwan Kim, Euisik Yoon, and György Buzsáki. Pyramidal Cell-Interneuron Circuit Architecture and Dynamics in Hippocampal Networks. *Neuron*, 96(2):505–520.e7, October 2017.
- W. Bryan Wilent and Douglas A. Nitz. Discrete place fields of hippocampal interneurons. *Journal of Neurophysiology*, 97(6): 4152–4161, June 2007.
- Robert U. Muller, Elizabeth Bostock, Jeffrey S. Taube, and John L. Kubie. On the directional firing properties of hippocampal place cells. *Journal of Neuroscience*, 14(12):7235–7251, 1994.
- Alon Rubin, Michael M. Yartsev, and Nachum Ulanovsky. Encoding of Head Direction by Hippocampal Place Cells in Bats. *The Journal of Neuroscience*, 34(3):1067, January 2014.
- Patricia Preston-Ferrer, Stefano Coletta, Markus Frey, and Andrea Burgalossi. Anatomical organization of presubicular head-direction circuits. *eLife*, 5:e14592, June 2016.
- Christian F. Doeller, Caswell Barry, and Neil Burgess. Evidence for grid cells in a human memory network. *Nature*, 463(7281):657–661, February 2010.
- Zé Henrique T. D. Góis and Adriano B. L. Tort. Characterizing Speed Cells in the Rat Hippocampus. *Cell Reports*, 25(7):1872–1884.e4, November 2018.
- Carey Y. L. Huh, Bénédicte Amilhon, Katie A. Ferguson, Frédéric Manseau, Susana G. Torres-Platas, John P. Peach, Stephanie Scodras, Naguib Mechawar, Frances K. Skinner, and Sylvain Williams. Excitatory Inputs Determine Phase-Locking Strength and Spike-Timing of CA1 Stratum Oriens/Alveus Parvalbumin and Somatostatin Interneurons during Intrinsically Generated Hippocampal Theta Rhythm. *The Journal of Neuroscience: The Official Journal of the Society for Neuroscience*, 36(25):6605–6622, 2016.
- Richard Kramis, Cornelius H. Vanderwolf, and Brian H. Bland. Two types of hippocampal rhythmical slow activity in both the rabbit and the rat: Relations to behavior and effects of atropine, diethyl ether, urethane, and pentobarbital. *Experimental Neurology*, 49(1): 58–85, October 1975.
- Robert S. Sainsbury, Arnold Heynen, and Christopher P. Montoya. Behavioral correlates of hippocampal type 2 theta in the rat. *Physiology & Behavior*, 39(4):513–519, January 1987.
- Tsai-Wen Chen, Trevor J. Wardill, Yi Sun, Stefan R. Pulver, Sabine L. Renninger, Amy Baohan, Eric R. Schreiter, Rex A. Kerr, Michael B. Orger, Vivek Jayaraman, Loren L. Looger, Karel Svoboda, and Douglas S. Kim. Ultra-sensitive fluorescent proteins for imaging neuronal activity. *Nature*, 499(7458):295–300, July 2013.
- Daniel A. Dombeck, Christopher D. Harvey, Lin Tian, Loren L. Looger, and David W. Tank. Functional imaging of hippocampal place cells at cellular resolution during virtual navigation. *Nature Neuroscience*, 13(11):1433–1440, November 2010.
- Joshua H. Siegle, Aarón Cuevas López, Yogi A. Patel, Kirill Abramov, Shay Ohayon, and Jakob Voigts. Open Ephys: an open-source, plugin-based platform for multichannel electrophysiology. *Journal of Neural Engineering*, 14(4):045003, 2017.
- Dmitriy Aronov and David W. Tank. Engagement of neural circuits underlying 2d spatial navigation in a rodent virtual reality system. *Neuron*, 84(2):442–456, October 2014.
- Marius Pachitariu, Carsen Stringer, Mario Dipoppa, Sylvia Schröder, L. Federico Rossi, Henry Dagleish, Matteo Carandini, and Kenneth D. Harris. Suite2p: beyond 10,000 neurons with standard two-photon microscopy. *bioRxiv*, page 061507, July 2017.
- Jakob Voigts, Joshua H. Siegle, Dominique L. Pritchett, and Christopher I. Moore. The flexDrive: an ultra-light implant for optical control and highly parallel chronic recording of neuronal ensembles in freely moving mice. *Frontiers in Systems Neuroscience*, 7, 2013.

Aaron van den Oord, Sander Dieleman, Heiga Zen, Karen Simonyan, Oriol Vinyals, Alex Graves, Nal Kalchbrenner, Andrew Senior, and Koray Kavukcuoglu. WaveNet: A Generative Model for Raw Audio. *arXiv:1609.03499 [cs]*, September 2016. arXiv: 1609.03499.

Andrew H. Fagg, Gregory W. Ojakangas, Lee E. Miller, and Nicholas G. Hatsopoulos. Kinetic Trajectory Decoding Using Motor Cortical Ensembles. *IEEE Transactions on Neural Systems and Rehabilitation Engineering*, 17(5):487–496, October 2009.

Karen Simonyan, Andrea Vedaldi, and Andrew Zisserman. Deep Inside Convolutional Networks: Visualising Image Classification Models and Saliency Maps. *arXiv:1312.6034 [cs]*, December 2013. arXiv: 1312.6034.

Chris Olah, Alexander Mordvintsev, and Ludwig Schubert. Feature Visualization. *Distill*, 2(11):e7, November 2017.

SUPPLEMENTARY MATERIAL

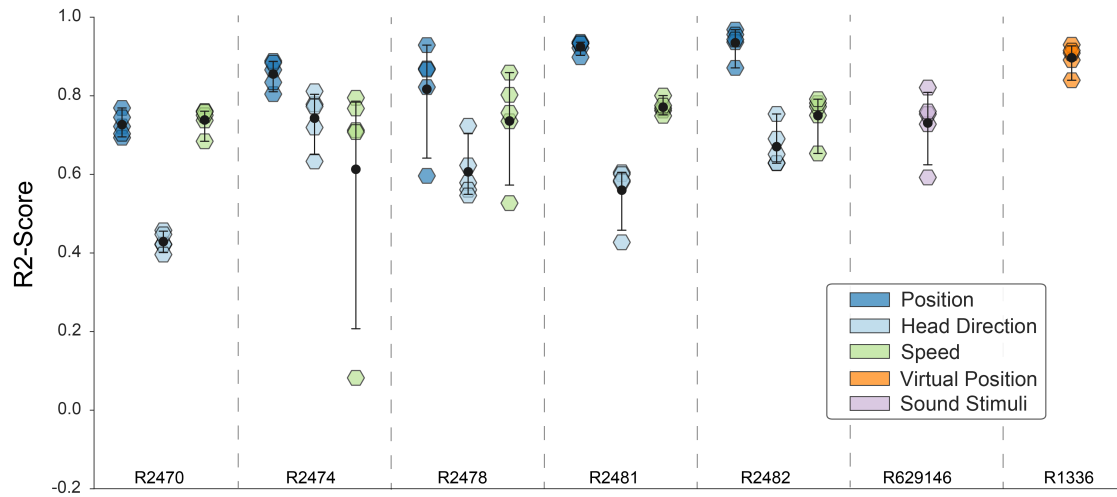


Figure S1: Model performance across different recording techniques and behaviours

We calculated the R²-score between the real behaviour and decoded behaviour for decoding of position, head direction, speed and auditory stimuli for tetrode and two-photon recordings. For all recordings, we use the raw data as input for the wavelet preprocessing and use the same architecture by only adjusting the last layer in order to incorporate different loss terms. The y-axis shows the R²-score, a measure of variance captured, with a max value of 1 and arbitrarily low negative values.

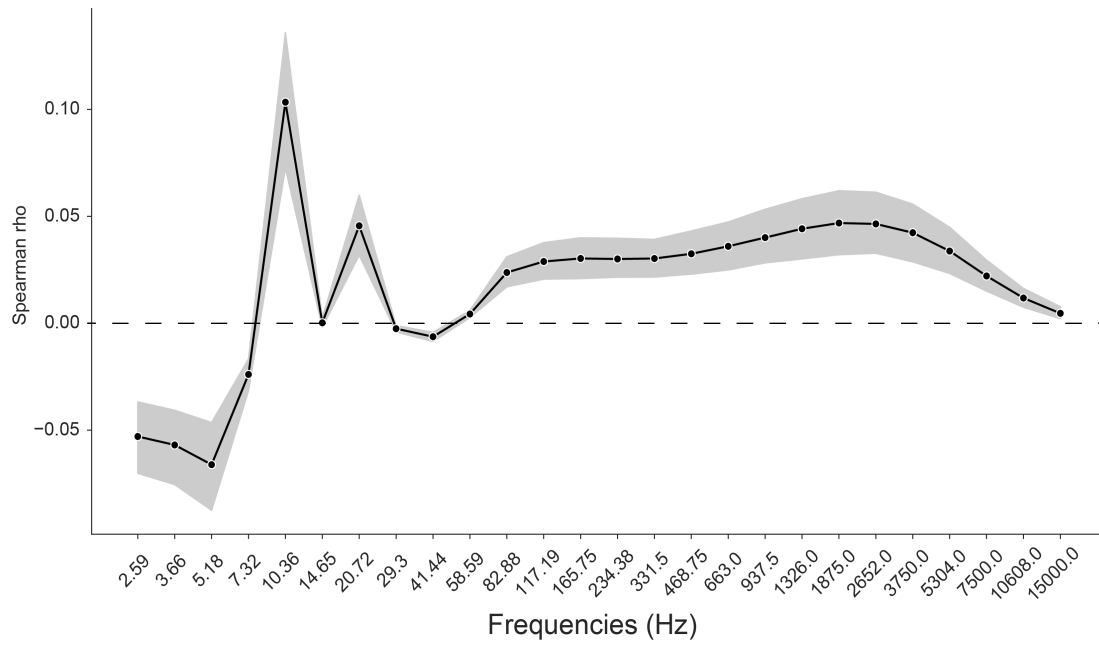


Figure S2: Speed-Power correlation

We calculated the Spearman correlation between the wavelet transformed electrophysiological signal and the instantaneous speed of the animal across frequencies from 2 to 15000Hz. Shaded area indicates 95% confidence interval (data from five rats).

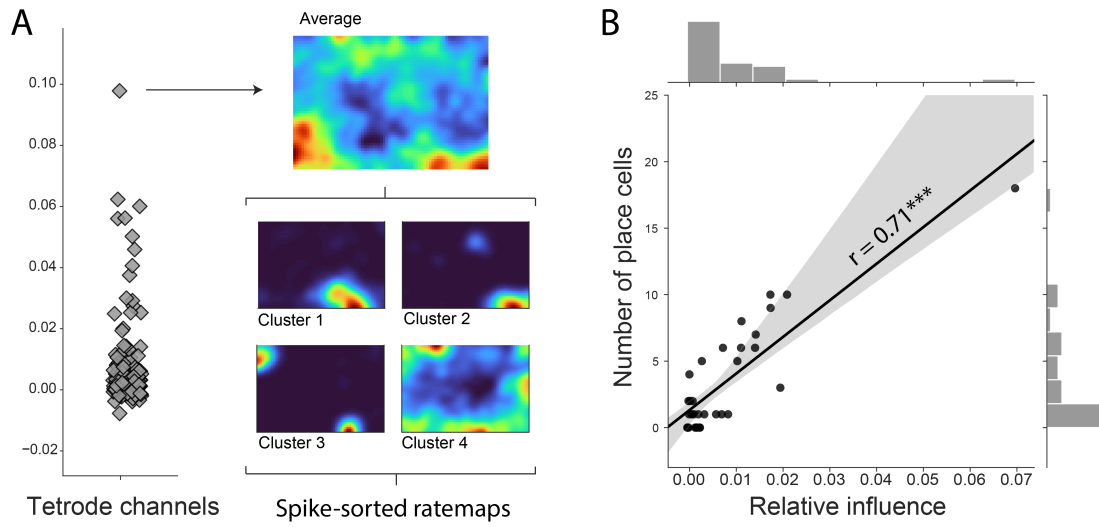


Figure S3: Influence of decoding across channels

(A) Channel influence scores for positional decoding (left). The most influential channel for the positional decoding has a high number of place cells (right). Average ratemap of all clusters (top, $n=21$) and four example clusters (bottom) shown. (B) Influence scores per tetrad (average influence over 4 channels) highly correlates with number of place cells on the tetrad, indicating that the network is correctly identifying place cells as the spatially most informative neural correlate.

Layer Type	Input Dimension	Kernel Size	Strides	Filters	
1	2D - Convolution	(64, 26, 128)	(3,3)	(2,1)	64
2	2D - Convolution	(32, 26, 128)	(3,3)	(1,2)	64
3	2D - Convolution	(32, 13, 128)	(3,3)	(2,1)	64
4	2D - Convolution	(16, 13, 128)	(3,3)	(1,2)	64
5	2D - Convolution	(16, 7, 128)	(3,3)	(2,1)	64
6	2D - Convolution	(8, 7, 128)	(3,3)	(1,2)	64
7	2D - Convolution	(8, 4, 128)	(3,3)	(2,1)	64
8	2D - Convolution	(4, 4, 128)	(3,3)	(1,2)	64
9	2D - Convolution	(4, 2, 128)	(3,2)	(1,2)	64
10	2D - Convolution	(4, 2, 64)	(3,2)	(1,2)	128
11	2D - Convolution	(4, 2, 32)	(3,2)	(1,2)	128
12	2D - Convolution	(4, 2, 16)	(3,2)	(1,2)	128
13	2D - Convolution	(4, 2, 8)	(3,2)	(1,2)	128
14	2D - Convolution	(4, 2, 4)	(3,2)	(1,2)	128
15	2D - Convolution	(4, 2, 2)	(3,2)	(1,2)	128
16	Fully Connected	(4, 512)	-	-	1024
17	Fully Connected	(4,)	-	-	2/1

Table S1: Layer by layer architecture of the convolutional model

Note that the first layers 1-8 share the weights over the channel dimension while layers 9-15 share the weights across the time dimension. Layers 9 to 15 depict the kernel sizes and strides for the tetrode recordings with 128 channels. For recordings with different number of channels we adjust the number of downsampling layers to match the dimension of layer 15. Order of dimensions: Time, Frequency, Channels.